Parametric modeling of wideband piezoelectric polymer sensors: Design for optoacoustic applications

A. Fernández Vidal, L. Ciocci Brazzano, C. L. Matteo, P. A. Sorichetti, and M. G. González

Parametric modeling of wideband piezoelectric polymer sensors: Design for optoacoustic applications

A. Fernández Vidal,[1] L. Ciocci Brazzano,[1,2] C. L. Matteo,[1,2] P. A. Sorichetti,[1] and M. G. González[1,2]

[1]Universidad de Buenos Aires, Facultad de Ingeniería, Grupo de Láser, Óptica de Materiales y Aplicaciones Electromagnéticas (GLOMAE), Paseo Colón 850, C1063ACV, Buenos Aires, Argentina
[2]Consejo Nacional de Investigaciones Científicas y Técnicas, (CONICET), Godoy Cruz 2290, C1425FQB Buenos Aires, Argentina

In this work, we present a three-dimensional model for the design of wideband piezoelectric polymer sensors which includes the geometry and the properties of the transducer materials. The model uses FFT and numerical integration techniques in an explicit, semi-analytical approach. To validate the model, we made electrical and mechanical measurements on homemade sensors for optoacoustic applications. Each device was implemented using a polyvinylidene fluoride thin film piezoelectric polymer with a thickness of 25 μm. The sensors had detection areas in the range between 0.5 mm^2 and 35 mm^2 and were excited by acoustic pressure pulses of 5 ns (FWHM) from a source with a diameter around 10 μm. The experimental data obtained from the measurements agree well with the model results. We discuss the relative importance of the sensor design parameters for optoacoustic applications and we provide guidelines for the optimization of devices. *Published by AIP Publishing.*
https://doi.org/10.1063/1.4986771

I. INTRODUCTION

Biomedical imaging using the optoacoustic (OA) effect is currently in full development, generating new technical approaches and applications.[1] In a typical OA configuration, the tissue is illuminated by nanosecond laser pulses. Pulse repetition rates are usually in the range of a few tens of Hertz, with energies around a few millijoules per pulse. For OA imaging, the pressure profiles generated by the optical excitation are captured with sensors that surround the area of interest. The image is finally obtained from the measured signal using reconstruction algorithms. These algorithms are significantly simplified if the sensor can be considered as an ideal one. We define an ideal point sensor as the limiting case where the output signal follows the instantaneous acoustic pressure (infinite bandwidth), and its characteristic size is much smaller than the shortest acoustic wavelength of interest. The effects of a non-ideal sensor on the image-reconstruction algorithms are quite important. For instance, the use of transducers with large detecting area can result in conspicuous image blurring and distortions in the reconstructed images.[2,3] In OA imaging, to attain spatial resolution of the order of microns, the spectral bandwidth of acoustic signals must be large, reaching up to hundreds of MHz. Moreover, in contrast to ultrasonic imaging (USI), the amplitudes of the OA signals are relatively low. In consequence, the use of high performance sensors is necessary to achieve high quality images in this and similar applications. In this context, a high performance sensor should have large bandwidth, high spatial resolution, and adequate sensitivity. There are two types of ultrasonic sensors: resonant and broadband (non-resonant). It follows from above that broadband sensors are required in OA imaging. Nevertheless, much of the ultrasound detection technology used nowadays involves resonating detectors due to the advantage of their higher sensitivity. However, the restriction of the bandwidth of the measured signal leads to an image with reduced resolution and artifacts.[4] In consequence, in order to obtain high performance sensors, different approaches have been implemented, notably the use of piezoelectric polymers.[5–10] It is possible to classified the sensors for OA applications in two main categories:[1] piezoelectric transducers, in which acoustic pressure is directly transformed into an electric signal, and optical detectors, which are sensitive to changes in the length of the optical path induced by pressure waves. The former type is the most commonly used and it is based on polymeric (broadband) or ceramic (resonant) materials such as those widely used in USI.[11,12] This technology has a relative low implementation cost and can be applied in high sensitivity measurements. Among piezoelectric polymers, the most popular ones are polyvinylidene fluoride (PVDF) and its copolymers, which have properties that are well suited for biological applications. These polymers have high dielectric and mechanical losses and relatively low pyro- and piezoelectric coefficients.[13] Therefore, their main application is in ultrasound receiving transducers.[14]

Models of broadband sensors for OA applications based on piezoelectric polymers are relatively scarce. We found a variety of works on the subject. Some of them assume ideal sensors for image reconstruction,[5–7] others propose very simplified models taking into account the thickness and the detection surface of the device,[8–10] and there are models that consider the temporal response of the detector.[2,15,16] Nevertheless, none of them fully takes into account the detailed characteristics of the polymeric material such as, the electrical and mechanical relaxation processes.

In a previous work,[17] we introduced a one-dimensional sensor model based on a thin film piezoelectric polymer, where the acoustic propagation is described by an equivalent transmission line model. In that work, the dependence of the electrical and mechanical material properties on frequency and temperature are included. This model provides a more complete description but it is valid under the excitation by plane acoustic waves and, in consequence, its applicability is limited to far field OA imaging.

In this work, we present a three-dimensional model for the design of wideband piezoelectric polymer sensors that explicitly includes the geometry and the properties of the sensor material. An explicit, semi-analytical approach enables the model to be simulated at a low computational cost, while maintaining a reasonable accuracy. This makes it easier to explore design alternatives for optimization purposes and also to take into account variations in the material properties and sensor geometry. This is a significant advantage in comparison to finite element modeling, which provides high accuracy but at the expense of a much longer simulation time, particularly when material relaxation processes are included.[18]

The paper is organized as follows. In Sec. II, we present a parametric model which integrates the wave propagation phenomena into the signal processing framework. In Sec. III, we detail the materials and methods used to validate the model described in Sec. II. We compare in Sec. IV the experimental data with the model results. In Sec. V, we explore different configurations and sensor design alternatives considering three aspects: the relative position between the acoustic source and the sensor, material properties, and sensor geometry. Finally, the conclusions of the work are given in Sec. VI.

II. PARAMETRIC MODEL

The modeled configuration is shown in Fig. 1. The source emits an acoustic pressure pulse with a gaussian temporal profile

$$p(t) = P_0 \cdot \exp(t^2/0.36 \cdot \tau_p^2), \tag{1}$$

where τ_p is the full width at half maximum characteristic time. Before reaching the surface of the PVDF film, the acoustic wave propagates first through the water and then into the glass. For the acoustic propagation calculations, the source can be considered as point-like. This is a reasonable assumption when the characteristic size of the source is much smaller than all the other relevant characteristics lengths of the problem. For the determination of the electrical charge q on the electrodes

of the PVDF film as a function of the acoustic pressure p, we propose the scheme shown in Fig. 2.

During manufacture, the PVDF film is stretched and then poled by applying an electric field in the direction perpendicular to the film. The poling direction is customarily indicated as the reference axis 3 (in this work, the z-axis) and the stretching direction in the plane of the film (the xy plane) is indicated as the reference axis 1 (x-axis). It is assumed that the acoustic wave only travels perpendicularly to the surface of the PVDF film behaving as a "normal reaction" material.[5] Under harmonic excitation of angular frequency ω and at constant temperature, the electromechanical intensive parameters can be related by[19]

$$d_{33}(\omega)^2/s_{33}(\omega) = \varepsilon_{33}^F(\omega) - \varepsilon_{33}^B(\omega), \tag{2}$$

where d_{33} is the piezoelectric coefficient, s_{33} is the elastic compliance at constant electric field, ε_{33}^F is the complex permittivity at free (zero stress) condition, and ε_{33}^B is the complex permittivity at blocked (zero strain) condition. Assuming that the polarization instantaneously follows the mechanical deformation, the difference between the free and blocked permittivities is proportional to the elastic compliance, i.e., d_{33} is proportional to s_{33},[20]

$$d_{33}(\omega) = \sigma_{33} s_{33}(\omega), \tag{3}$$

where σ_{33} is the equivalent surface charge density of remnant polarization. It is a real constant within the relevant frequency range. Using the method described in Ref. 20, ε_{33}^F, ε_{33}^B, and σ_{33} can be determined. In Ref. 21, we show that the permittivity of the PVDF can be described by the Havriliak-Negami (HN) function.[22] Therefore, in the frequency range of interest, d_{33} can be written as

$$d_{33}(\omega) = \frac{\varepsilon_F^\infty - \varepsilon_B^\infty}{\sigma_{33}} + \frac{\frac{\Delta\varepsilon_{33}^F - \Delta\varepsilon_{33}^B}{\sigma_{33}}}{(1 + (i\tau_0\omega)^\alpha)^\beta} =$$
$$= d_{33}^\infty + \frac{\Delta d_{33}}{(1 + (i\tau_0\omega)^\alpha)^\beta}, \tag{4}$$

where ε_F^∞ and ε_B^∞ are the limiting values of the permittivity at high frequencies, $\Delta\varepsilon_{33}^F$ and $\Delta\varepsilon_{33}^B$ are the relaxation strength (in both cases, the supra-indexes ^{F} and ^{B} refer to the free and blocked conditions, respectively), τ_0 is the characteristic relaxation time, and α and β are shape parameters that describe the broadening of the relaxation peak. The shape parameters are related to symmetric (α) and asymmetric (β) broadening of the relaxation peak, and they are both positive numbers
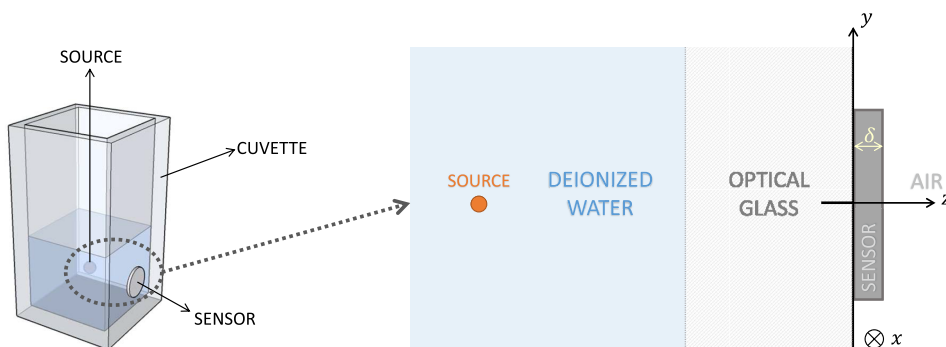

FIG. 1. Scheme of the modeled configuration. The cutaway diagram is not to scale.

$$p((x,y,z),t) \rightarrow \boxed{d_{33}(\omega)} \xrightarrow{D((x,y,z),t)} \boxed{W(\omega, \Gamma_a, \Gamma_g, \delta, a_\delta)} \xrightarrow{\sigma_p((x,y),t)} \boxed{\iint_A dx\, dy} \rightarrow q(t)$$
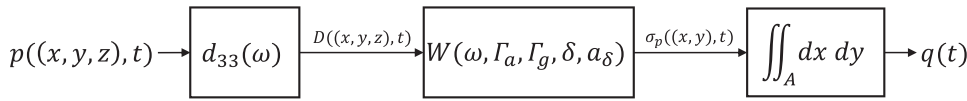
FIG. 2. Block diagram of the proposed model to calculate the electric charge on the sensor.

(for physical relaxation processes, the product $\alpha\beta$ must always be less than 1).[22]

Given the instantaneous pressure $p(r, t)$, the electric displacement $D(r, t)$ can then be calculated by the time convolution between $p(r, t)$ and $d_{33}(t)$, where $d_{33}(t)$ is the impulse response of the piezoelectric polymer, i.e., the inverse Fourier transform of Eq. (4). In this work, it is assumed that the pressure p has most of its energy spectrum concentrated in a frequency band well within the range where d_{33} is defined by Eq. (4).

Then, the electric charge density σ_p can be approximated by taking the average of D along the z axis. This is possible because the quasi-static description is appropriate from the electrical point of view due to the enormous difference between the velocities of propagation of the electrical and mechanical disturbances in the material.[17]

The acoustic reflections at the rear and front surfaces of the sensor, together with the thickness and acoustic attenuation of the piezoelectric film, are described by the function $w(z)$ (see Fig. 3),

$$w(z, \Gamma_a, \Gamma_g, \delta, a_\delta) = [\,\Pi(\frac{z}{\delta}) + \Gamma_a\, \Pi(\frac{z-\delta}{\delta}) +$$
$$+ \Gamma_a \Gamma_g\, \Pi(\frac{z-2\delta}{\delta})]\, e^{-a_\delta z}, \qquad (5)$$

where δ is the thickness of the film; $\Pi(\frac{z}{\delta})$ is a rectangular window between 0 and δ; Γ_g and Γ_a are the reflection coefficients of the interfaces PVDF-glass (front) and PVDF-air (rear), respectively; and a_p is the attenuation factor of acoustic propagation through the film. This model assumes that Γ_g, Γ_a, and a_p are frequency independent. The successive reflections of the acoustic wave between the front and rear faces of the sensor are replaced by the equivalent propagation through several layers. Equation (5) considers only the first two reflections. If necessary, further reflections can be taken into account in a straightforward way (i.e., for low attenuation piezoelectrics).

The electric charge density is calculated from $D(r, t)$ and the function $w(z)$ given by Eq. (5). Since the function $w(z)$ has bounded support, and assuming that the sound velocity v_p in the film does not depend on the frequency, σ_p can be calculated by performing a convolution,

$$\sigma_p((x,y),t) =$$
$$= \frac{1}{\delta} \int_{-\infty}^{\infty} w(t'v_p, \Gamma_a, \Gamma_g, \delta, \alpha)\, D((x,y,0),\, t-t')\, v_p\, dt'. \qquad (6)$$

In Eq. (6), we made the change of variables $t = z/vp$. In this way, σ_p is expressed as time-domain convolutions between p, d_{33}, and w.

Given a point source of pressure waves, each point on the sensor surface is excited by a signal with the same temporal profile but scaled in amplitude and with a different delay. Assuming that each point on the surface behaves as a point sensor and that this detector can be approximated as a linear and time invariant (LTI) system, it follows that all the points on the surface of the sensor behave as identical LTI systems. This allows to calculate $\sigma_p((x,y),t)$ for the different values of x and y, using $\sigma_p((0,0),t)$ from Eq. (6) and applying scaling, k, and delay, Δt, functions,

$$\sigma_p((x,y),t) = k(r)\, \sigma_p((0,0),\, t - \Delta t(r)). \qquad (7)$$

As seen from Fig. 4, the $(0, 0)$ point corresponds to the projection of the source position on the sensor plane. From the model configuration, k and Δt may be calculated, under the geometrical acoustics approximation, using elementary ray-tracing techniques (see Fig. 4),

$$\Delta t(r) = \frac{\frac{d_G}{\cos(\theta_G(r))} - d_G}{v_G} + \frac{\frac{d_W}{\cos(\theta_W(r))} - d_W}{v_W}, \qquad (8)$$

$$k(r) = T_{WG} \frac{r_o}{l_W + l_G} \cos(\theta_G(r)) =$$
$$= T_{WG} \frac{d_W + d_G}{\frac{d_G}{\cos(\theta_G(r))} + \frac{d_W}{\cos(\theta_W(r))}} \cos(\theta_G(r)), \qquad (9)$$

where $r = (x^2 + y^2)^{1/2}$; v_W and v_G are the sound velocity in water and glass, respectively; θ_W and θ_G are the Snell angles of water and glass interfaces, respectively; and T_{WG} is the transmission coefficient in pressure at the interface water-glass given by[23]

$$T_{WG} = \frac{2\rho_G v_G \cos(\theta_W)}{\rho_W v_W \cos(\theta_G) + \rho_G v_G \cos(\theta_W)}, \qquad (10)$$

where ρ_G and ρ_W are the mass densities of glass and water, respectively. In these expressions, it was assumed that in the
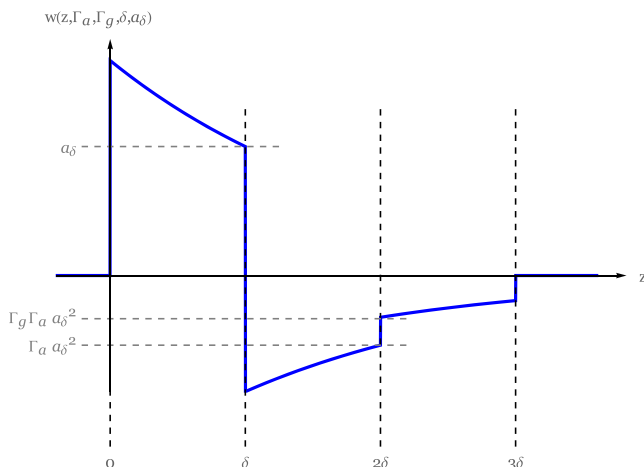

FIG. 3. Spatial window used to describe the reflections on the rear back (PVDF-air) and on the front face (PVDF-glass) of the sensor, including the attenuation of the acoustic signal. Values used in this plot: $a_p = 0.6$; $\Gamma_a = 0.9$; $\Gamma_g = 0.62$.
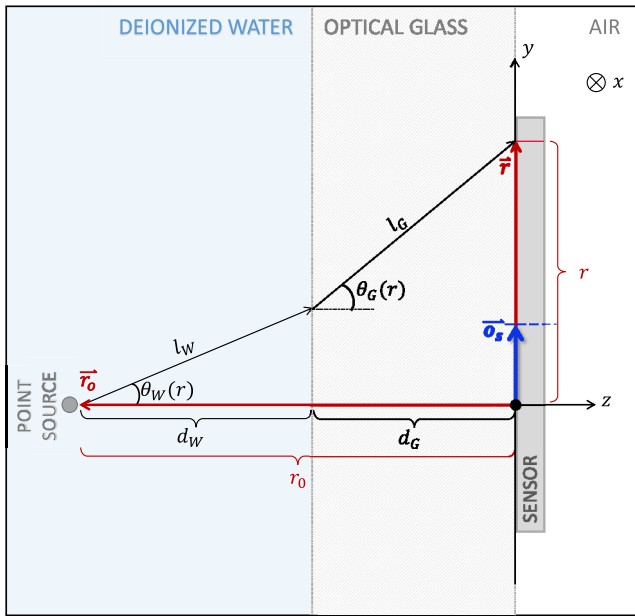
FIG. 4. Path of the acoustic signal through the water-glass interface. The source is at a distance r_0 from the sensor. A circular cross section sensor is assumed.

liquid-solid interface, the transmission coefficient of the longitudinal waves is real and greater than that of the shear waves and also that practically does not depend on the angle θ_W.[23] These hypotheses are fulfilled for the geometrical and material parameters of the setup described in this work. As explained above, the PVDF film behaves as a "normal reaction" material. Therefore, the $\cos(\theta_G(r))$ factor takes into account the oblique incidence of the pressure signal.

In the case of a circular sensor not aligned with the pressure source, a radial positioning parameter o_s (see Fig. 4) is defined. For the case of a non-circular sensor, two parameters, o_{sx} and o_{sy}, are defined to represent the positioning on each axis separately (see Fig. 5).

Finally, $q(t)$ is calculated by the following integral:

$$q(t) = \iint_A \sigma_p((x,y), t) \, dx \, dy. \tag{11}$$
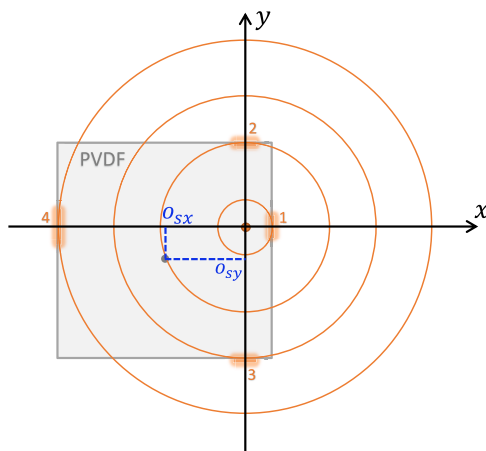

FIG. 5. Scheme of the positioning parameters for the case of a non-circular sensor.

It is important to remark that the model presented in this work involves explicit, mostly analytical calculations. This simplifies the treatment of material relaxation processes and significantly speeds up the simulations.

III. MATERIALS AND METHODS

To validate the model, we made several sensors of different detection areas in the range between 0.5 mm² and 35 mm². Each sensor was implemented using a PVDF thin film piezoelectric polymer (PIEZOTECH CORP, 25 μm thick, metalized on both sides) attached to a spectroscopy-quality quartz cuvette and encapsulated in a standard BNC (see Fig. 6). In all the measurements, the cuvette was filled with deionized water and its temperature was monitored using a calibrated thermocouple. The water temperature was kept at 300.0 K $\pm$ 0.1 K and the room temperature at 300 K $\pm$ 1 K. A transimpedance amplifier (Femto HCA-100M-50K-C) was used to amplify the signal detected by the sensor.

Electrical and acoustic measurements were carried out on each sensor. The material properties and sensor assembly were checked by measuring its electrical admittance. These measurements were made with a bridge circuit excited by a synthesized signal generator (Agilent N9310) in the range from 100 kHz to 90 MHz. The output signals from the bridge were captured by a fast digitizer (Agilent U2702, 0.5 Gs/s, 200 MHz) and processed with an FFT routine. The bridge was calibrated with measurements in the "open" condition and also with a reference capacitor (ceramic C0G dielectric, 47 pF). The low-loss reference capacitor was previously characterized with a vector network analyzer to ensure that its self-resonant frequency was over 250 MHz, well above the intended measurement range. The details of the measurement method and the calibration procedures are given in Ref. 21.

The frequency response of the amplifier was independently determined at frequencies up to 200 MHz using a network analyzer. Moreover, the frequency response of each sensor connected to the amplifier was also measured, to check that it was not affected. In all cases, the bandwidth of the amplifier exceeded the frequency range of interest and, in consequence, its gain and phase response could be considered as ideal.

Optoacoustic measurements employed a setup similar to that used on the study of laser-induced bubble generation on gold nanoparticles.[24,25] A Nd:YAG laser with a second harmonic generator (Continuum Minilite I, 532 nm, 5 ns, 10 Hz) and a converging lens (10 mm) were used to generate a gaussian pressure signal on a target submerged in the cuvette. The target is a copper wire with a diameter around 10 μm. Its position in the cuvette is adjusted using a XYZ translation stage. The lens focuses the laser beam on the copper wire, into a spot with a diameter of 10 μm, thus providing a roughly spherical irradiated volume. In this way, as indicated in Sec. II, within the range of frequency studied in this work, the irradiated target may be regarded as a point source of pressure waves. The temporal profile of the pressure pulses was checked by a wideband interferometric method described in the work of Riobo *et al.*[26] The sensor output was amplified with the transimpedance amplifier, digitized by an oscilloscope (Tektronix TDS 2024,
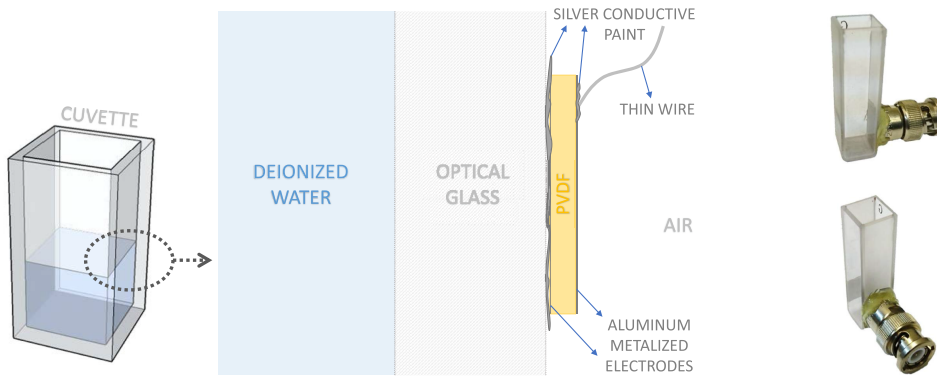
FIG. 6. Left: out-of-scale sensor scheme. Right: picture of one of the sensors implemented.

2 GS/s, 200 MHz) and processed on a personal computer. The oscilloscope trigger signal was obtained from the laser Q-switch pulse. A sample of the main laser beam was taken by a beamsplitter to measure the laser pulse energy with a pyroelectric detector (Coherent LMP10).

The numerical simulations were carried out with a program developed in the Wolfram Mathematica (WA) environment.

IV. SIMULATIONS AND EXPERIMENTAL VALIDATION

The sensors described in Sec. III were modeled using the parameter values from Table I. The adjustable parameters were chosen to give the best fitting to experimental results (in the least square sense). The initial values related to the PVDF film parameters were obtained from Ref. 20. The initial value of v_p is an average sound speed in the PVDF film, weighted by the spectral energy density of the source pulse (in the frequency range of interest). The initial values of the acoustic reflection coefficients were calculated from the PVDF properties given in Ref. 20, assuming plane waves. The initial value of v_G was determined from direct measurements in the cuvettes used in this paper.

For the sake of computational efficiency, the time-domain convolution between p, d_{33}, and w [Eq. (6)] is calculated as a product in the frequency domain and then the Inverse Fast Fourier Transform (IFFT) algorithm is used to obtain the result in the time domain. In the IFFT algorithm, we choose a maximum frequency of at least five times the spectral width of the pressure pulse (more than 99% of its energy). The frequency-domain sampling interval is chosen as $1/(40\tau_0)$. This ensures that the calculated time-domain response is in all cases much longer than the relaxation time of the piezoelectric response. The integral of Eq. (11) was calculated using the *NIntegrate* WA function.

As explained in Sec. III, the transimpedance amplifier in this work may be considered as ideal. Therefore, the measured value of the charge, $q(t)$, may be obtained as the time integral of the output signal of the amplifier.

In order to ensure the consistency of the results, all parameter fittings were performed following the same sequential procedure, as shown in Fig. 7 for the case of a square sensor: (A) the size of the sensor was estimated based on the relative distance between the positive peak and the midpoint between the negative peaks; (B) the positioning parameters, o_{sx} and o_{sy}, were adjusted to provide the correct spacing between the negative peaks; (C) the widths of the positive and the negative peaks were fitted by varying the value of v_p; and (D) the signal amplitude was fitted by carefully adjusting the reflection and attenuation coefficients. This fitting sequence was chosen based on the influence that the parameters have on the sensor response as described in Sec. V. It must be stressed that in all cases, the fitted values of the adjustable parameters were very close to their initial values.
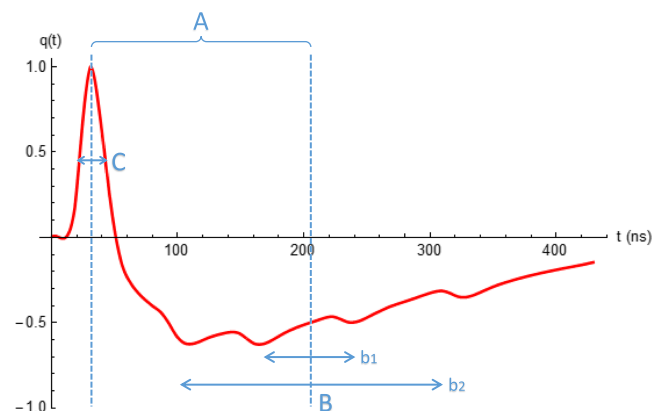
TABLE I. Fixed and adjustable parameters used in the simulation where ρ_0 is the PVDF density, v_A is the air sound velocity, and r_s and l_s are the radius or side of the sensor, respectively.

Fixed parameters		Adjustable parameters	
	Reference value		Initial value
δ	25 μm	τ_0	140 ns
Δd_{33}	34.5 pC/N	v_p	2200 m/s
d_{33}^{∞}	1.1 pC/N	Γ_g	0.65
α	0.5	Γ_a	0.99
β	0.68	a_p	0.66
σ_{33}	7.7 μC/cm^2	v_G	3570 m/s
v_A	347 m/s	d_W	2.5 mm
v_W	1500 m/s	τ_p	5 ns
ρ_0	1780 kg/m^3	r_s, l_s	$\geq$0.8 mm, $\leq$4 mm
d_G	1 mm	o_s, o_{sx}, o_{sy}	<2 mm

FIG. 7. Fitting steps for a square sensor. This example assumes $o_{sx} < o_{sy}$. In this way, the distances b_1 and b_2 can be adjusted through o_{sx} and o_{sy}, respectively.
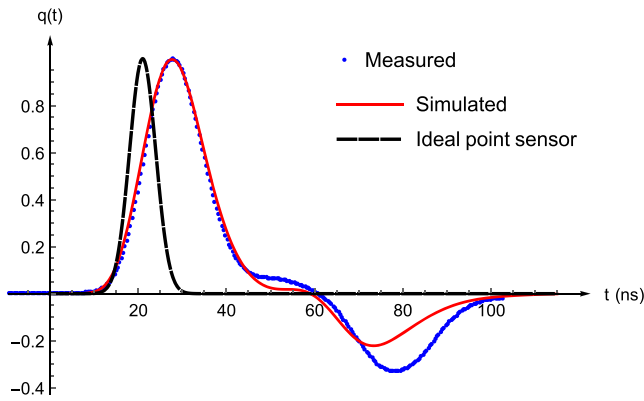
FIG. 8. Simulated (solid) and measured (dots) values of the normalized electric charge for a square sensor with a side length of 0.8 mm. The response of an ideal point sensor is also shown (dashes).

FIG. 10. Simulated (solid) and measured (dots) values of the normalized electric charge for a square sensor with a side length of 4 mm. The positioning parameters are $o_{sx} = 0.9$ mm and $o_{sy} = 0.26$ mm. The response of an ideal point sensor is also shown (dashes).

Figures 8–11 show the experimental data (dots) and the simulated response (solid) together with the response of an ideal point sensor (dashes), for different sensor sizes and source positions.

The smallest sensor studied was square, with a side length of 0.8 mm (see Fig. 8). The final values of the fitted parameters are $l_s = 0.8$ mm; $\tau_0 = 140$ ns; $v_p = 2240$ m/s; $a_p = 0.6$; $\Gamma_a = 0.99$; $\Gamma_g = 0.55$; $v_G = 3603$ m/s; $\tau_p = 5$ ns; $d_W = 2.69$ mm; $o_{sx} = 0.42$ mm; $o_{sy} = 0$ mm. The adjusted values of the positioning on each axis agree well with those measured directly from the translation stage.

The simulation agrees very well with the experimental data up to the end of the main (positive) pulse. The negative part of the signal is mainly due to the reflection at the back of the sensor (PVDF-air interface). It can be seen that in the latter part of the negative pulse, the amplitude of the simulated response differs from the experimental data. This is due to the reflections of the acoustic wave on the lateral boundaries of the sensor, which are superimposed with the main reflection coming from the back of the sensor. This edge effect is not included in the present model; for instance, the elastic and piezoelectric anisotropy of PVDF is neglected. The effect of the edge reflections is clearly seen in larger sensors. Figure 9 shows the experimental and simulation data of the electric
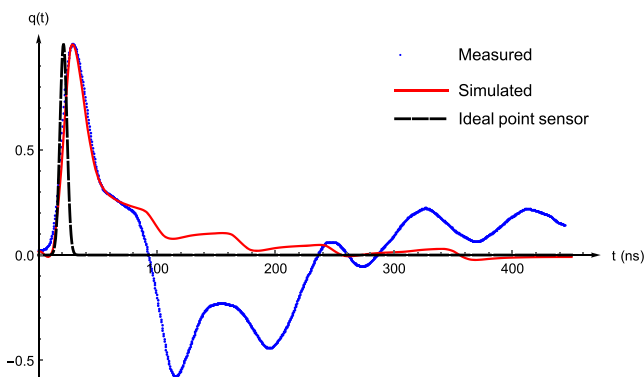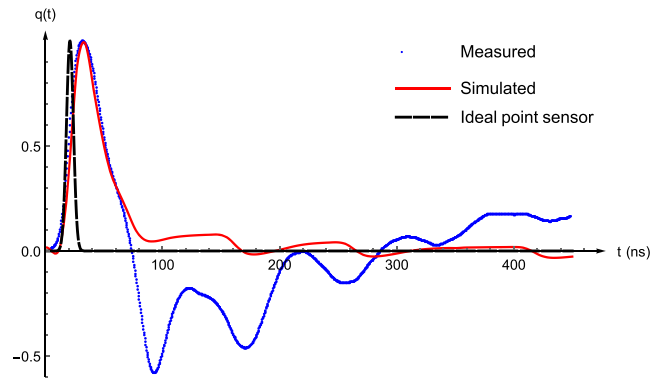
charge in a square sensor with a side of 4 mm. The adjusted parameter values are $l_s = 3.5$ mm; $\tau_0 = 140$ ns; $v_p = 2209$ m/s; $a_p = 0.65$; $\Gamma_a = 0.99$; $\Gamma_g = 0.65$; $v_G = 4547$ m/s; $\tau_p = 5$ ns; $d_W = 2.22$ mm; $o_{sx} = 0.66$ mm; $o_{sy} = 0.2$ mm. As indicated above, these values are very close to the initial values and those of the previous example. The difference of the value of v_G is due the use of a quartz cuvette instead of optical glass.

The agreement between the experimental data and the simulation is very good in the initial part of the signal (positive pulse). In the latter part, the effect of the reflections on the four sides of the sensor is clearly seen. The measured timing of the reflections agrees well with the simulation, but the amplitudes are clearly different. The limitations in the modeling of the edge effects are also indicated by the difference between the geometrical length of the sensor side (4 mm) and the adjusted value ($l_s = 3.5$ mm). As an additional check, the same sensor was measured and simulated in different positions relative to the acoustic source (i.e., changing the positioning parameters). The results are shown in Figs. 10 and 11. It must be remarked that, after the adjustment process, the values of the other simulation parameters remained practically unchanged. The modifications of the relative position between the sensor and the source originate changes on the reflections times that are adequately predicted by the model.
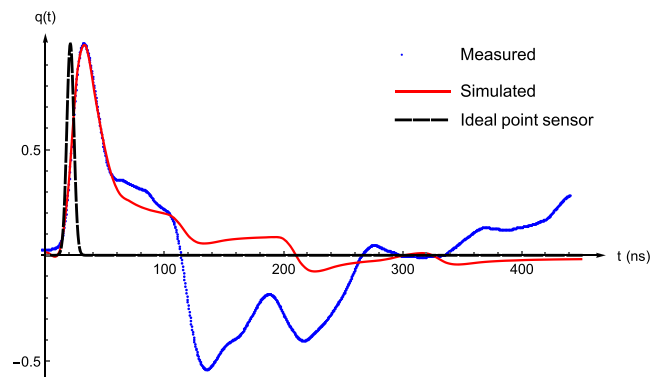

FIG. 9. Simulated (solid) and measured (dots) values of the normalized electric charge for a square sensor with a side length of 4 mm. The positioning parameters are $o_{sx} = 0.66$ mm and $o_{sy} = 0.2$ mm. The response of an ideal point sensor is also shown (dashes).

FIG. 11. Simulated (solid) and measured (dots) values of the normalized electric charge for a square sensor with a side length of 4 mm. The positioning parameters are $o_{sx} = 0.55$ mm and $o_{sy} = 0$ mm. The response of an ideal point sensor is also shown (dashes).

As it may be seen from Figs. 8–11, the response of the devices clearly differs from the limiting case of an ideal point sensor. This is due to the finite size, relaxation processes, and acoustic reflections that are unavoidable in a physical realizable piezoelectric sensor.

V. DISCUSSION

The model presented in Sec. II makes it possible to explore different configurations and sensor design alternatives. In this work, three aspects are considered: the relative position between the acoustic source and the sensor, material properties, and sensor geometry. Unless indicated, the simulation parameters are the same of Table I.

A. Acoustic source-sensor relative position

Figure 12 plots the response of a circular sensor ($r_s = 1.5$ mm) for three values of the radial positioning parameter o_s. From the figure it may be seen that the initial part of the signal (positive pulse) is not altered by changes in this parameter for this sensor size (we will discuss this later). However, the effect of the reflections at the boundaries of the sensor is clearly modified. When $o_s = 0$ mm, there is a single reflected pulse (the incident acoustic wave reaches all the points at the sensor boundary simultaneously). When o_s increases, there are two reflected pulses, originated by reflections at opposite sides of the sensor (the two points that are closest and farthest from $(0, 0)$).

B. Material properties

The relaxation time of the piezoelectric polymer has a direct impact on the amplitude of the output signal. The plot (dots) in Fig. 13 describes the response of a circular sensor made of a material of negligible relaxation time ($\tau_0 = 0$ ns), and its other properties being the same as those of PVDF. In the same figure, the calculated response for $\tau_0 = 20$ ns (dashes) and $\tau_0 = 140$ ns (solid) is also shown. The effect on the high frequency components of the output signal is noticeable, both on the amplitude and the trailing edges.

Ultrasonic attenuation is another important material parameter for the sensor design. As the attenuation increases,
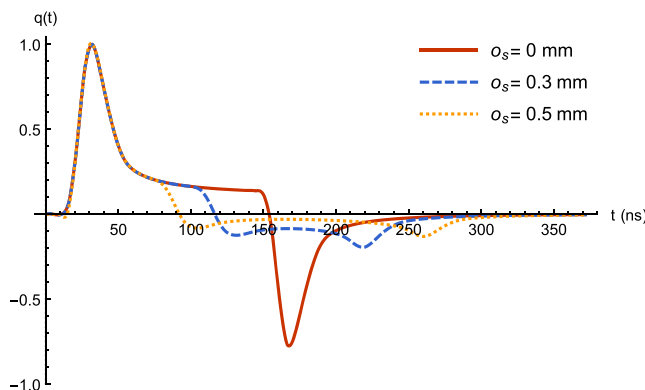

FIG. 13. Simulation of the variation of $q(t)$ on a circular sensor ($r_s = 1.5$ mm) as a function of the characteristic relaxation time of the PVDF film.

the peak amplitude of the signal decreases, together with the effect of the reflections on the back of the sensor. The simulation results for different values of the average attenuation coefficient are shown in Fig. 14.

C. Sensor geometry

The thickness of the piezoelectric film is a critical parameter for the sensor impulse response. Roughly speaking, the characteristic time of the impulse response, in the limit of high reflections ($\Gamma_a \rightarrow 1$), is determined by the propagation delay of the acoustic wave through the piezoelectric film, t_p (i.e., the ratio between the film thickness and the average sound velocity in it). The responses for several values of δ are presented in Fig. 15 for $\Gamma_a = 0.99$, where it can be seen that the main pulse width increases with the sensor thickness. Moreover, the rise time and the delay to the peak of the main pulse show the same trend.

In the limit $\Gamma_a \rightarrow 1$, the reflections of the lateral boundaries of the sensor have a noticeable effect on the initial response for sensors of small radii ($r_s < 1$ mm), as shown in Fig. 16. For larger sizes, the reflections occur after the main pulse has ended and therefore, the main pulse is not superimposed with the reflections.

The acoustic reflections at the back of the sensor influence the overall response regardless of its size. As discussed above, in the limit of high reflection ($\Gamma_a \rightarrow 1$), the width of the

FIG. 12. Simulation of the variation of $q(t)$ on a circular sensor ($r_s = 1.5$ mm) as a function of the positioning between the sensor and the acoustic source.
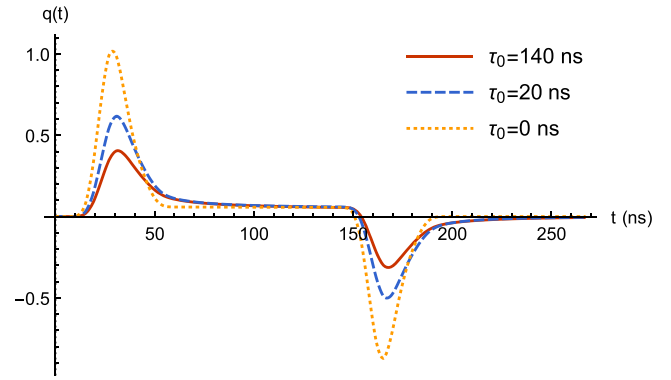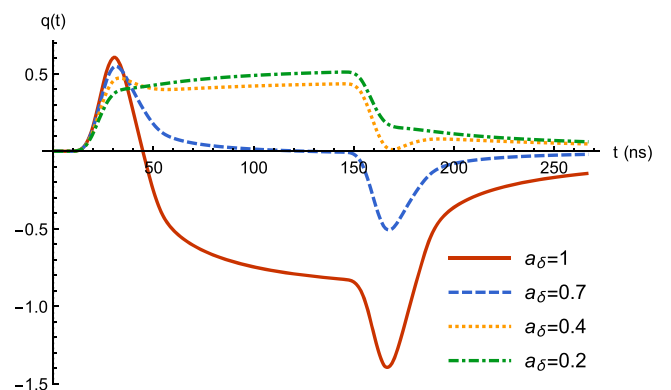

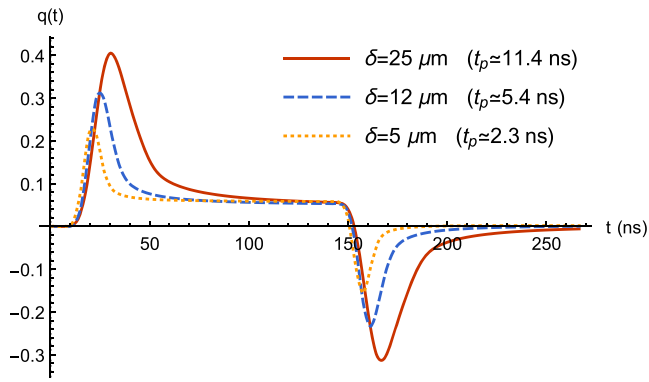FIG. 14. Simulation of the variation of $q(t)$ on a circular sensor ($r_s = 1.5$ mm) as a function of the acoustic attenuation.

FIG. 15. Simulation of the variation of $q(t)$ on a circular sensor ($r_s = 1.5$ mm) as a function of the thickness of the PVDF film.

FIG. 18. Simulation of the variation of $q(t)$ on a sensor as a function of its radius with a suitable backing ($\Gamma_a = 0.1$).

initial (positive) pulse depends on the film thickness and the lateral reflections. With an adequate design and selection of the backing material, Γ_a can be substantially reduced. In that case, the impulse response of the sensor is determined by its lateral dimensions. This may be seen by taking the limit $\Gamma_a \to 0$ in Eq. (5), where the width of the time convolution window depends only on the film thickness,

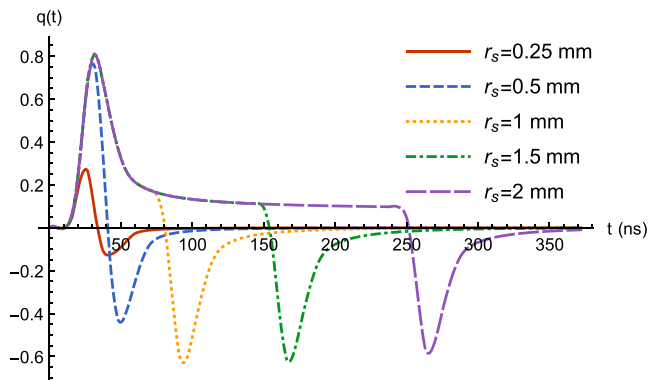$$w(z, 0, \Gamma_g, \delta, a_\delta) = \Pi(\frac{z}{\delta})e^{-a_\delta z}. \qquad (12)$$

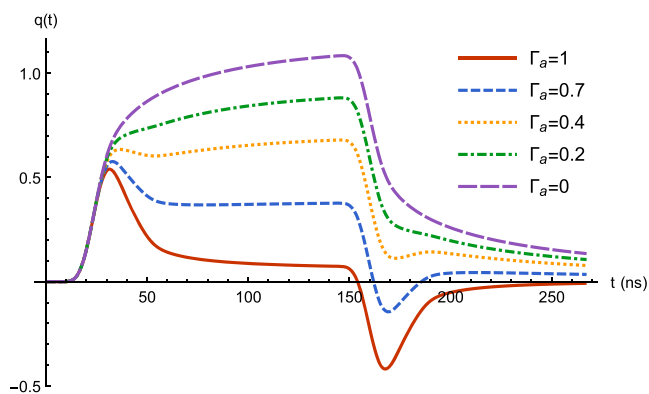FIG. 16. Simulation of the variation of $q(t)$ on a sensor as a function of its radius.

FIG. 17. Simulation of the variation of $q(t)$ on a circular sensor ($r_s = 1.5$ mm) as a function of the reflection coefficient of the back face of the sensor.
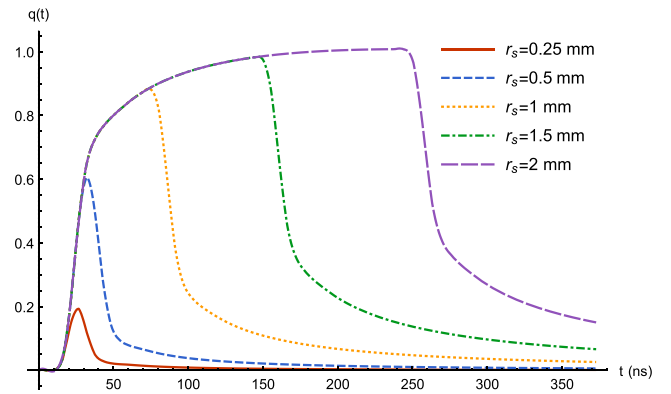
Therefore, the output signal depends on the sensor geometry through the integral of the response over the sensor area, Eq. (11). This is clearly seen in Fig. 17.

The influence of the piezoelectric film thickness is more noticeable as the lateral dimension of the sensor decreases. In most applications, however, the lateral dimensions will be substantially greater than the film thickness, thus being the limiting parameter for the temporal width of the impulse response (Fig. 18).

VI. CONCLUSIONS

The analysis and design of optoacoustic imaging systems involve wave propagation and signal processing aspects. The model presented in this work integrates the wave propagation phenomena into the signal processing framework through an explicit, mostly analytic approach. In this way, the influence of the material parameters and sensor geometry may be explored to provide design criteria, with a significantly lower computational effort compared with finite element methods. Furthermore, parametric modeling together with Monte Carlo methods makes it straightforward to take into account the statistical dispersion of material properties[27–29] and physical dimensions of the devices. This will be the subject of future works.

The model was validated by measurements in sensors of different sizes. The simulations and experimental results highlight the differences with the response of an ideal point sensor, due to finite size, relaxation processes, and acoustic reflections. From the parametric modeling, it follows that acoustic reflections (in the back and edges of the sensor) have a direct impact on the response. However, the ultimate limits of the sensor performance are given by the material properties: ultrasonic attenuation and piezoelectric relaxation. Interestingly, the effects of the acoustic reflections in the rear of the sensor may be reduced not only by a suitable backing but also taking into account the ultrasonic attenuations and thickness of the piezoelectric film. The properties of piezoelectric polymers, such as PVDF, make unnecessary the complete elimination of the reflections ("perfect" backing) to achieve satisfactory performance. In contrast, this is often an issue in ceramic transducers.[30]

In summary, the model makes possible to ascertain the relative importance of the sensor design parameters for a given application and also provides a guide for the device optimization.

ACKNOWLEDGMENTS

[1] C. Lutzweiler and D. Razansky, "Optoacoustic imaging and tomography: Reconstruction approaches and outstanding challenges in image performance and quantification," Sensors **13**, 7345–7384 (2013).

[2] K. Wang, S. A. Ermilov, R. Su, H.-P. Brecht, A. A. Oraevsky, and M. A. Anastasio, "An imaging model incorporating ultrasonic transducer properties for three-dimensional optoacoustic tomography," IEEE Trans. Med. Imaging **30**, 203–214 (2011).

[3] A. Rosenthal, V. Ntziachristos, and D. Razansky, "Model-based optoacoustic inversion with arbitrary-shape detectors," Med. Phys. **38**, 4285–4295 (2011).

[4] A. Rosenthal, V. Ntziachristos, and D. Razansky, "Acoustic inversion in optoacoustic tomography: A review," Curr. Med. Imaging Rev. **9**, 318–336 (2013).

[5] M. Haltmeier, O. Scherzer, P. Burgholzer, and G. Paltauf, "Thermoacoustic computed tomography with large planar receivers," Inverse Probl. **20**, 1663 (2004).

[6] S. Gratt, K. Passler, R. Nuster, and G. Paltauf, "Photoacoustic section imaging with an integrating cylindrical detector," Biomed. Opt. Express **2**, 2973–2981 (2011).

[7] E. Blumenröther, O. Melchert, M. Wollweber, and B. Roth, "Detection, numerical simulation and approximate inversion of optoacoustic signals generated in multi-layered PVA hydrogel based tissue phantoms," Photoacoustics **4**, 125–132 (2016).

[8] G. Paltauf, R. Nuster, and P. Burgholzer, "Characterization of integrating ultrasound detectors for photoacoustic tomography," J. Appl. Phys. **105**, 102026 (2009).

[9] B. Reyes-Ramírez, C. García-Segundo, and A. García-Valenzuela, "An examination of polyvinylidene fluoride capacitive sensors as ultrasound transducer for imaging applications," Meas. Sci. Technol. **25**, 055109 (2014).

[10] M. Jaeger, J. Niederhauser, M. Hejazi, and M. Frenz, "Diffraction-free acoustic detection for optoacoustic depth profiling of tissue using an optically transparent polyvinylidene fluoride pressure transducer operated in backward and forward mode," J. Biomed. Opt. **10**, 024035-1–024035-7 (2005).

[11] S. Manohar, A. Kharine, J. C. G. van Hespen, W. Steenbergen, and T. G. van Leeuwen, "The Twente Photoacoustic Mammoscope: System overview and performance," Phys. Med. Biol. **50**, 2543 (2005).

[12] W. Xia, D. Piras, J. C. G. van Hespen, S. vanVeldhoven, C. Prins, T. G. van Leeuwen, W. Steenbergen, and S. Manohar, "An optimized ultrasound detector for photoacoustic breast tomography," Med. Phys. **40**, 032901 (2013).

[13] L. F. Brown, "Design considerations for piezoelectric polymer ultrasound transducers," IEEE Trans. Ultrason., Ferroelectrics Freq. Control **47**, 1377–1396 (2000).

[14] Q. X. Chen and P. A. Payne, "Industrial applications of piezoelectric polymer transducers," Meas. Sci. Technol. **6**, 249 (1995).

[15] M. Haltmeier and G. Zangerl, "Spatial resolution in photoacoustic tomography: Effects of detector size and detector bandwidth," Inverse Probl. **26**, 125002 (2010).

[16] M. A. Caballero, J. Gateau, X.-L. Déan-Ben, and V. Ntziachristos, "Model-based optoacoustic image reconstruction of large three-dimensional tomographic datasets acquired with an array of directional detectors," IEEE Trans. Med. Imaging **33**, 433–443 (2014).

[17] M. G. González, P. A. Sorichetti, and G. D. Santiago, "Modeling thin-film piezoelectric polymer ultrasonic sensors," Rev. Sci. Instrum. **85**, 115005 (2014).

[18] *Modeling and Simulation in Polymers*, edited by P. Gujrati and A. Leonov (John Wiley and Sons, 2010), Chap. 7, 8, and 11.

[19] K. Uchino, "Loss mechanisms in piezoelectrics: How to measure different losses separately," IEEE Trans. Ultrason., Ferroelectrics Freq. Control **48**, 307 (2001).

[20] M. G. Gonzalez, P. A. Sorichetti, L. Ciocci Brazzano, and G. D. Santiago, "Electromechanical characterization of piezoelectric polymer thin films in a broad frequency range," Polym. Test. **37**, 163 (2014).

[21] L. Ciocci Brazzano, P. A. Sorichetti, G. D. Santiago, and M. G. Gonzalez, "Broadband dielectric characterization of piezoelectric poly(vinylidene flouride)thin films between 278 K and 308 K," Polym. Test. **32**, 1186 (2013).

[22] S. Havriliak and S. Negami, "A complex plane analysis of α-dispersions in some polymer systems," J. Polym. Sci., Part C: Polym. Symp. **14**, 99 (1966).

[23] L. Brekhovskikh, *Waves in Layered Media* (Academic Press, 1980), pp. 41–47.

[24] M. G. Gonzalez, X. Liu, R. Niessner, and C. Haisch, "Strong size-dependent photoacoustic effect on gold nanoparticles by laser-induced nanobubbles," Appl. Phys. Lett. **96**, 174104 (2010).

[25] E. Acosta, M. G. Gonzalez, P. A. Sorichetti, and G. D. Santiago, "Laser-induced bubble generation on a gold nanoparticle: A nonsymmetrical description," Phys. Rev. E **92**, 062301-1–062301-5 (2015).

[26] L. M. Riobo, F. E. Veiras, P. A. Sorichetti, and M. T. Garea, "Wideband quad optical sensor for high-speed sub-nanometer interferometry," Appl. Opt. **56**, 397–403 (2017).

[27] *Materials With Complex Behaviour: Modelling, Simulation Testing and Applications*, edited by A. Brochier, M. Aufray, W. Possart, L. da Silva, and H. Altenbach (Springer-Verlag, 2010), pp. 99–123.

[28] L. Jaulin and E. Walter, "Guaranteed nonlinear parameter estimation from bounded-error data via interval analysis," Math. Comput. Simul. **35**, 123–137 (1993).

[29] L. Ciocci Brazzano, L. J. Pellizza, P. A. Sorichetti, and C. L. Matteo, "A Bayesian method for analysing relaxation spectra," Comput. Phys. Commun. **198**, 22–30 (2016).

[30] S. M. Ji, J. H. Sung, C. Y. Park, and J. S. Jeong, "Phase-canceled backing structure for lightweight ultrasonic transducer," Sens. Actuators, A **260**, 161–168 (2017).